Chirp management in silicon-graphene electro absorption modulators

V. SORIANELLO,[1] G. CONTESTABILE,[2] M. MIDRIO,[3] M. PANTOUVAKI,[4] I. ASSELBERGS,[4] J. VAN CAMPENHOUT,[4] C. HUYGHEBAERTS,[4] A. D'ERRICO,[5] P. GALLI,[6] AND M. ROMAGNOLI[1,*]

[1]*Consorzio Nazionale per le Telecomunicazioni (CNIT), National Laboratory of Photonic Networks, Via G. Moruzzi 1, 56124 Pisa, Italy*
[2]*Consorzio Nazionale per le Telecomunicazioni (CNIT), Scuola Superiore Sant'Anna, Via G. Moruzzi 1, 56124 Pisa, Italy*
[3]*Consorzio Nazionale per le Telecomunicazioni (CNIT), University of Udine, Via delle Scienze 206, 33100 Udine, Italy*
[4]*IMEC, Kapeldreef 75, 3001 Leuven, Belgium*
[5]*Ericsson Research, Via G. Moruzzi 1, 56124 Pisa, Italy*
[6]*Nokia Bell Labs, Via Energy Park 14, 20871 Vimercate, Italy*
[*]marco.romagnoli@cnit.it

Abstract: We study the frequency chirp properties of graphene-on-silicon electro-absorption modulators (EAMs). By experimentally measuring the chirp of a 100 μm long single layer graphene EAM, we show that the optoelectronic properties of graphene induce a large positive linear chirp on the optical signal generated by the modulator, giving rise to a maximum shift of the instantaneous frequency up to 1.8 GHz. We exploit this peculiar feature for chromatic-dispersion compensation in fiber optic transmission thanks to the pulse temporal lensing effect. In particular, we show dispersion compensation in a 10Gb/s transmission experiment on standard single mode fiber with temporal focusing distance (0-dB optical-signal-to-noise ratio penalty) of 60 km, and also demonstrate 100 km transmission with a bit error rate largely lower than the conventional Reed-Solomon forward error correction threshold of 10^{-3}.

OCIS codes: (130.3120) Integrated optics devices; (130.4110) Modulators; (130.2035) Dispersion compensation devices; (060.0060) Fiber optics and optical communications.

References and links

1. A. C. Ferrari, F. Bonaccorso, V. Fal'ko, K. S. Novoselov, S. Roche, P. Bøggild, S. Borini, F. H. Koppens, V. Palermo, N. Pugno, J. A. Garrido, R. Sordan, A. Bianco, L. Ballerini, M. Prato, E. Lidorikis, J. Kivioja, C. Marinelli, T. Ryhänen, A. Morpurgo, J. N. Coleman, V. Nicolosi, L. Colombo, A. Fert, M. Garcia-Hernandez, A. Bachtold, G. F. Schneider, F. Guinea, C. Dekker, M. Barbone, Z. Sun, C. Galiotis, A. N. Grigorenko, G. Konstantatos, A. Kis, M. Katsnelson, L. Vandersypen, A. Loiseau, V. Morandi, D. Neumaier, E. Treossi, V. Pellegrini, M. Polini, A. Tredicucci, G. M. Williams, B. H. Hong, J. H. Ahn, J. M. Kim, H. Zirath, B. J. van Wees, H. van der Zant, L. Occhipinti, A. Di Matteo, I. A. Kinloch, T. Seyller, E. Quesnel, X. Feng, K. Teo, N. Rupesinghe, P. Hakonen, S. R. T. Neil, Q. Tannock, T. Löfwander, and J. Kinaret, "Science and technology roadmap for graphene, related two-dimensional crystals, and hybrid systems," Nanoscale **7**(11), 4598–4810 (2015).
2. F. Bonaccorso, Z. Sun, T. Hasan, and A. C. Ferrari, "Graphene photonics and optoelectronics," Nat. Photonics **4**(9), 611–622 (2010).
3. A. Pospischil, M. Humer, M. M. Furchi, D. Bachmann, R. Guider, T. Fromherz, and T. Mueller, "CMOS-compatible graphene photodetector covering all optical communication bands," Nat. Photonics **7**(11), 892–896 (2013).
4. Y. Hu, M. Pantouvaki, J. Van Campenhout, S. Brems, I. Asselberghs, C. Huyghebaert, P. Absil, and D. Van Thourhout, "Broadband 10 Gb/s operation of graphene electro-absorption modulator on silicon," Laser Photonics Rev. **10**(2), 307–316 (2016).
5. A. H. Castro Neto, F. Guinea, N. M. R. Peres, K. S. Novoselov, and A. K. Geim, "The electronic properties of graphene," Rev. Mod. Phys. **81**(1), 109–162 (2009).
6. G. W. Hanson, "Dyadic Green's function and guided surface waves for a surface conductivity model of Graphene," J. Appl. Phys. **103**(6), 064302 (2008).

7. K. F. Mak, M. Y. Sfeir, Y. Wu, C. H. Lui, J. A. Misewich, and T. F. Heinz, "Measurement of the optical conductivity of graphene," Phys. Rev. Lett. **101**(19), 196405 (2008).
8. M. Liu, X. Yin, E. Ulin-Avila, B. Geng, T. Zentgraf, L. Ju, F. Wang, and X. Zhang, "A graphene-based broadband optical modulator," Nature **474**(7349), 64–67 (2011).
9. M. Liu, X. Yin, and X. Zhang, "Double-layer graphene optical modulator," Nano Lett. **12**(3), 1482–1485 (2012).
10. C. T. Phare, Y. D. Lee, J. Cardenas, and M. Lipson, "Graphene electro-optic modulator with 30 GHz bandwidth," Nat. Photonics **9**(8), 511–514 (2015).
11. F. H. L. Koppens, T. Mueller, P. Avouris, A. C. Ferrari, M. S. Vitiello, and M. Polini, "Photodetectors based on graphene, other two-dimensional materials and hybrid systems," Nat. Nanotechnol. **9**(10), 780–793 (2014).
12. I. Goykhman, U. Sassi, B. Desiatov, N. Mazurski, S. Milana, D. de Fazio, A. Eiden, J. Khurgin, J. Shappir, U. Levy, and A. C. Ferrari, "On-chip integrated, silicon-graphene plasmonic Schottky photodetector, with high responsivity and avalanche photogain," Nano Lett. **16**(5), 3005–3013 (2016).
13. V. Sorianello, G. De Angelis, T. Cassese, M. Midrio, M. Romagnoli, M. Moshin, M. Otto, D. Neumaier, I. Asselberghs, J. Van Campenhout, and C. Huyghebaert, "Complex effective index in graphene-silicon waveguides," Opt. Express **24**(26), 29984–29993 (2016).
14. C. Xu, Y. Jin, L. Yang, J. Yang, and X. Jiang, "Characteristics of electro-refractive modulating based on Graphene-Oxide-Silicon waveguide," Opt. Express **20**(20), 22398–22405 (2012).
15. J. Gosciniak and D. T. H. Tan, "Theoretical investigation of graphene-based photonic modulators," Sci. Rep. **3**(1), 1897 (2013).
16. M. Midrio, P. Galli, M. Romagnoli, L. C. Kimerling, and J. Michel, "Graphene-based optical phase modulation of waveguide transverse electric modes," Photonics Res. **2**(3), A34 (2014).
17. A. Phatak, Z. Cheng, C. Qin, and K. Goda, "Design of electro-optic modulators based on graphene-on-silicon slot waveguides," Opt. Lett. **41**(11), 2501–2504 (2016).
18. P. P. Absil, P. De Heyn, H. Chen, P. Verheyen, G. Lepage, M. Pantouvaki, J. De Coster, A. Khanna, Y. Drissi, D. Van Thourhout, and J. Van Campenhout, "Imec iSiPP25G silicon photonics: a robust CMOS-based photonics technology platform," Proc. SPIE **9367**, 93670V (2015).
19. X. Li, W. Cai, J. An, S. Kim, J. Nah, D. Yang, R. Piner, A. Velamakanni, I. Jung, E. Tutuc, S. K. Banerjee, L. Colombo, and R. S. Ruoff, "Large-area synthesis of high-quality and uniform graphene films on copper foils," Science **324**(5932), 1312–1314 (2009).
20. J. Kang, D. Shin, S. Bae, and B.H. Hong, Nanoscale **4**, "Graphene transfer: key for applications," 5527 (2012).
21. V. Sorianello, M. Midrio, and M. Romagnoli, "Design optimization of single and double layer graphene phase modulators in SOI," Opt. Express **23**(5), 6478–6490 (2015).
22. G. P. Agrawal, Nonlinear Fiber Optics, Elsevier 2007.
23. M. Nedeljkovic, R. Soref, and G. Z. Mashanovich, "Free-Carrier electrorefraction and electroabsorption modulation predictions for Silicon over the 1−14μm infrared wavelength range," IEEE Photonics J. **3**(6), 1171–1180 (2011).
24. M. Romagnoli, P. Franco, R. Corsini, A. Schiffini, and M. Midrio, "Time-domain Fourier optics for polarization-mode dispersion compensation," Opt. Lett. **24**(17), 1197–1199 (1999).
25. J. D. Downie, "Relationship of Q penalty to eye-closure penalty for NRZ and RZ signals with signal-dependent noise," J. Lightwave Technol. **23**(6), 2031–2038 (2005).
26. T. Broderick and S. Boscolo, "Simple eye closure penalty estimate for amplitude noise-degraded signals, in optical transmission," Proc. SPIE **7136**, 71362D (2008).
27. Lumerical Solutions, Inc., http://www.lumerical.com/tcad-products/mode/

1. Introduction

Graphene is nowadays extensively studied for a large range of applications [1] and has been recently proven very suitable for photonic integrated circuits [2]. In particular, Graphene is a material compatible for complementary metal-oxide semiconductor (CMOS) Silicon (Si) photonic technologies [3,4], providing unique optoelectronic properties [5–7]. Graphene enables the improvement of a number of photonic functions in the Si photonic platform, e.g. electro-absorption modulation [3,8–10], and detection [4,11,12]. Regarding optical modulation, the complex effective refraction index of Graphene on Si waveguides has been recently measured and theoretically fitted [13]. The resulting data show that, by electrically gating the Fermi level of Graphene, the waveguide absorption changes with a simultaneous large electro-refractive effect (effective index change) [14–17]. This result suggests a large optical phase chirping during intensity modulation in Graphene-based electro-absorption modulators (EAMs). Although several Graphene on Si EAMs have been reported [3,8–10], frequency chirp and dispersion tolerance have not been studied and characterized in practical transmission applications yet.

In this letter, for the first time to the best of our knowledge, we report a detailed study of the chirp properties of Graphene EAMs. We experimentally characterize the phase of the

optical signals generated by the Graphene modulator and observed that the phase temporal profile has the same shape and duration of the amplitude envelope, but with inverted sign. Moreover, we show that the frequency chirp due to the phase change is a function of the driving voltage. In order to test the effect of the modulator chirp in a fiber transmission, we performed transmission experiments at 1550 nm wavelength over standard single mode fiber (SMF) links of different lengths. We find that the signal pre-chirping introduced by the EAM extends the reach of the transmission at 10 Gb/s beyond 100 km compensating for the fiber dispersion distortions and inter-symbol interference.

2. Fabrication and theory

The device we characterize is a single layer Graphene (SLG) on Si waveguide EAM similar to the one reported in [3]. The modulator is based on a 100 μm long Si photonic waveguide with SLG transferred on top of the Si waveguide core. Figure 1(b) shows an optical microscope picture of the fabricated device. In the inset of Fig. 1(b), we also report a SEM picture of a detail of the Graphene layer on top of the Si waveguide.
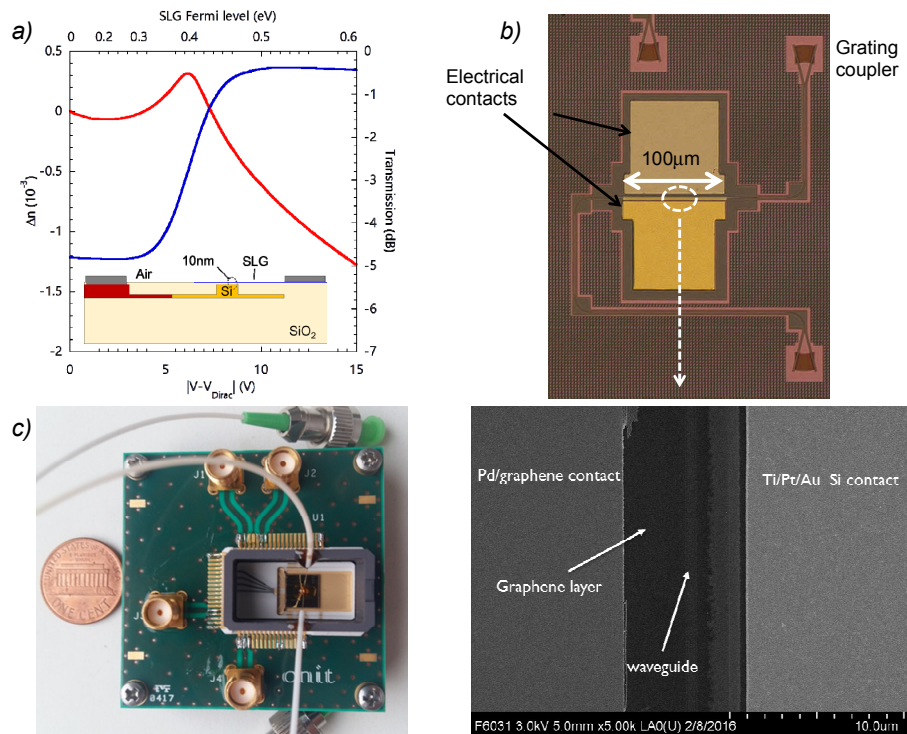

Fig. 1. a) Simulated effective index change (red curve, left axis) and transmission (blue curve, right axis) at λ = 1550 nm of the 100 μm-long SLG on Si EAM, versus the applied voltage |V-V_{DIRAC}|. In the inset the device cross section (orange: lightly doped Si waveguide; red: highly doped Si contact regions; grey: metal contacts). (b) Optical microscope image of the device used for measurement with SEM image of a detail of the active region on top of the waveguide. We indicate the Pd contact on graphene, the Graphene layer and the Ti/Pt/Au contact on Si. (c) Picture of a packaged EAM sample.

The Si photonic waveguide was realized within the IMEC iSiPP25G silicon on insulator (SOI) platform [18]. The Si ridge waveguide is designed to support a single transverse electric (TE) in-plane polarized optical mode with a core cross-section of 480 nm x 220 nm and 60 nm slab. The waveguide is boron doped to reduce the Si electrode resistance and allow high-speed operation. The waveguide SiO_2 top cladding is thinned down to 10 nm on the top of the waveguide core. SLG is grown by chemical vapor deposition (CVD) on copper foil

[19], and then transferred on the waveguide by standard wet transfer [20]. Graphene was shaped through optical lithography and oxygen ashing. Metal contacts were placed by metal lift-off on the SLG and Si with separate processes: Palladium (Pd) is used for the SLG, while Si is contacted with a stack of Titanium (Ti)/Platinum (Pt)/Gold (Au). The 10 nm-thick layer of SiO_2 insulates Graphene from the Si waveguide core and forms a Silicon-Insulator-Graphene (SIG) capacitor. Fermi Level on Graphene may be changed by applying a voltage across the SIG capacitor [13]. Standard single polarization grating couplers having 5 dB insertion loss at 1550 nm are also included in the device design for input and output vertical fiber coupling. A packaged version of the EAM with input and output fibers mounted on a dedicated PCB is reported in Fig. 1(c).

Figure 1(a) shows a cross section of the EAM along with the simulated effective index change (red curve, left axis) and transmissivity (blue curve, right axis) at 1550 nm of the fundamental TE mode of the EAM versus the applied voltage $|V\text{-}V_{DIRAC}|$. V_{DIRAC} is the flat-band voltage corresponding to the charge-neutral Dirac point. The curves are obtained using the numerical approach discussed in [21] with a scattering parameter of 100 fs.

We can observe that, as the voltage applied to the SIG capacitor increases, carriers accumulate on the SLG causing the shift of Fermi level towards higher energies [21]. When the Graphene Fermi level is driven beyond the Pauli blocking condition (> 0.4 eV at 1550 nm), the effective refraction index change, and the optical transmissivity have an opposite dependence with respect to the applied voltage: this means that the optical signal phase decreases when the transmitted power increases. Moreover, in a certain range of Fermi levels (Graphene carrier doping), the phase changes linearly and follows the transmitted power profile. Considering a single voltage pulse applied to the EAM, the generated optical pulse should exhibit a temporal phase with the same profile as the optical intensity but with an inverse sign. This means that the instantaneous frequency chirp increases linearly from the trailing to the leading edge of the pulse around its peak.

As mentioned above, the chirp depends on the variation of charges accumulated on the SLG. However, when carriers accumulate on the SLG, they also accumulate in the Si waveguide underneath. Through the plasma-dispersion effect, these carriers contribute to the change of the effective index and chirp. In particular, both SLG and Si induce a reduction of the effective index when populated by carriers. As we demonstrated in a previous work [21], the SLG offers the main contribution to the effective index change, while Si is responsible of about 1/3 of the overall effect. Moreover, larger effect is expected in the double layer Graphene modulator, where the voltage is applied between the SLG on top of an undoped Si waveguide. In such device, the effective index variation is roughly improved by a factor of two [21], which means that a larger chirp would be obtained.

3. Experimental characterization of chirp

We characterized the EAM in terms of static transmission versus applied voltage and electro-optical bandwidth; results are reported in Fig. 2.
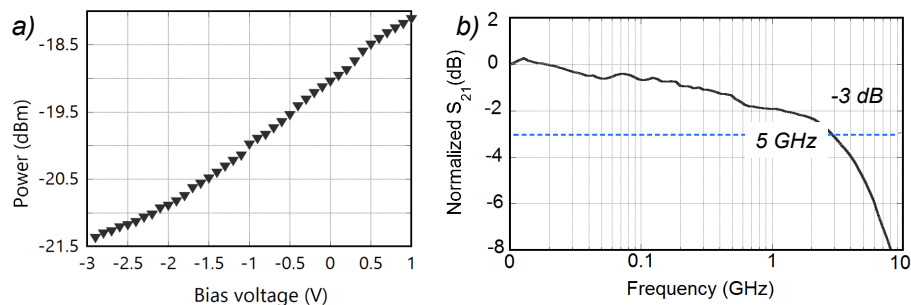

Fig. 2. (a) Static characterization of the SLG EAM output optical power versus applied voltage. (b) Normalized electro-optical S21 parameter versus frequency.

We used a continuous-wave external cavity laser (CW-ECL) at 1550 nm as a light source coupled to the EAM by means of the integrated Si grating couplers. The modulator shows a modulation efficiency of about 1 dB/V (Fig. 2(a)). The range of applied bias in Fig. 2(a) includes the voltage shift due to the Dirac point ($V_{Dirac} \sim -7V$), which is caused by the doping induced in the graphene transfer process.

Figure 2(b) shows the modulator frequency response. The modulator exhibits 3-dB bandwidth of 5 GHz at −1V bias voltage (Fig. 2(b)) which is limited by the electrical RC response of the device (mainly because of the high SLG contact resistance).

We characterized the frequency chirp of the modulated optical signals using a complex spectrum analyzer (Apex AP2440). For the pulse characterization, we generate a sequence of isolated '1' pulses at 10 Gb/s using an electrical peak-to-peak driving voltage of 2.7 V and a bias voltage of −1V. Figure 3 shows the characterization results. The pulses have a bell shape due to low pass filtering of the modulator. The 1/e HWHM (half width half maximum) pulse duration is $T_0 \approx 54ps$ (correspondingly the full width half maximum is $T_{FWHM} = 90ps$).
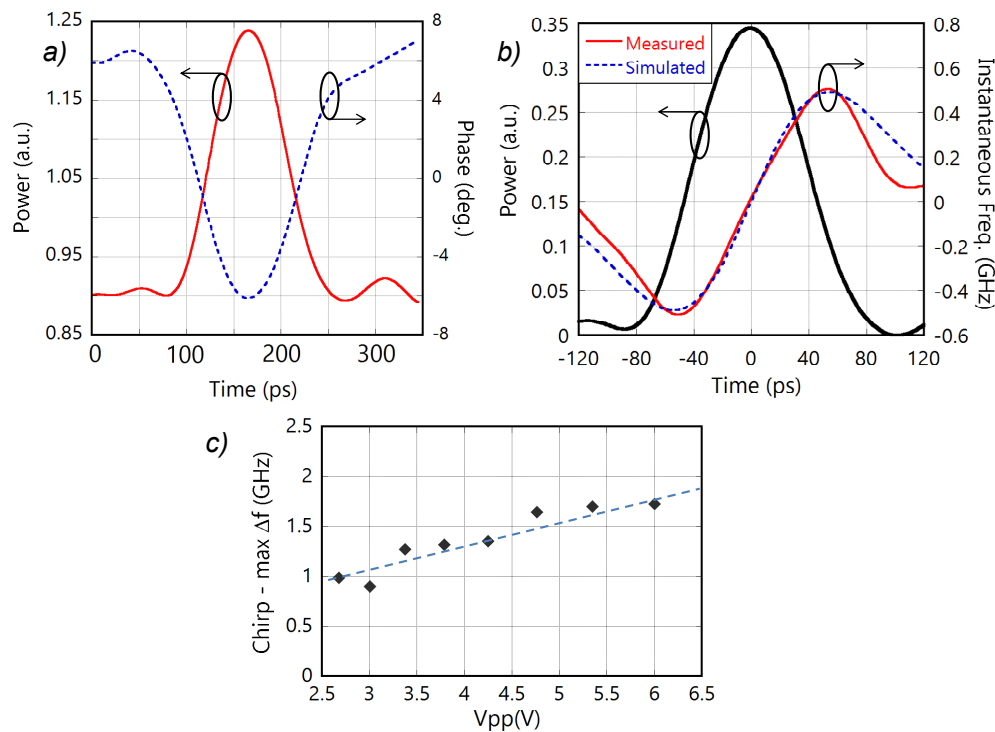

Fig. 3. (a) Measured amplitude (red line) and phase (blue line) pulse profile versus time. (b) Pulse amplitude profile (black line), measured instantaneous instantaneous frequency (red line) and simulated instantaneous frequency (blue dashed line) versus time. See Appendix A for details of the fitting curve. (c) Maximum span of the instantaneous frequency deviation versus applied V_{pp}.

We find that the power and phase profiles of an isolated pulse (red and blue lines, respectively, in Fig. 3(a)) exhibit, as expected from the discussion before, same shape but opposite sign, i.e. when pulse amplitude increases the phase decreases and vice versa. The pulse is positively chirped, i.e. it exhibits an instantaneous frequency that increases toward the trailing edge [22]. The maximum deviation of the instantaneous frequency is in the order of 1 GHz at 2.7 V_{pp} driving voltage and $V_{bias} = -1V$ (see the solid red line in Fig. 3(b)). From numerical fitting (blue dashed line Fig. 3(b)) and in the approximation of Gaussian pulse, we extract a positive chirp parameter C of 0.27 (for details see Appendix A, the relation between

the maximum deviation of the instantaneous frequency and chirp parameter C is reported in Eq. (8)). The amount of phase modulation and the corresponding chirp is a function of the applied voltage as shown in Fig. 1(a). Figure 3(c) shows the maximum span of the instantaneous frequency deviation versus the applied peak-to-peak voltage: it raises from 1 GHz at 2.7 V_{pp} to 1.8 GHz at 6 V_{pp}. Those values have been directly measured similarly to Fig. 3(b) by using a complex spectrum analyzer. As shown in Fig. 1(a), when above 0.45 eV the transmitted power starts to saturate whereas the phase decreases almost linearly. This make possible, in that voltage region, signal chirp management while keeping almost constant the extinction ratio (ER).

4. Transmission through an optical fiber link: theory, numerical simulations and experimental results

Standard single mode fibers have anomalous group velocity dispersion ($\beta_2<0$) and then dispersion compensation require positive frequency pre-chirping of the signal. Graphene can provide the correct frequency chirping and this is a straightforward element of novelty achievable in graphene EAM modulators. For comparison in Si p-n junctions modulators the applied signal voltage induces a change in the free carrier concentration of the waveguide core, which results in a variation of both the refractive index and absorption (as described by the empirical formulas proposed by Soref et al. [23]). This effect is similar to what discussed for the SLG EAM with the difference that in Soref's formulas the refractive index and the absorption have an opposite dependence on the change of free carrier concentration, i.e. as a function of the applied voltage. Hence, the signals generated by plasma dispersion effect in Si p-n junction waveguides exhibits a negative chirp, i.e. the opposite of what happens with Graphene. In addition, the free carrier effect is not as efficient as Graphene for electro-absorption modulation in Si photonics.

We performed numerical simulations of the effect of the pre-chirping introduced by Graphene EAMs on chromatic dispersion compensation for SMFs. We used the simplified Gaussian amplitude modulation model of [22] (see Appendix A for details) and found that with a positive chirp parameter *C*, signal pulse duration can be compressed from an initial value T_0 down to $T_0/\sqrt{(1 + C^2)}$. This effect can be regarded as a temporal lens, where chirp is a phase modulation in the time domain that is converted into pulse temporal squeezing through fiber chromatic dispersion [24]. The propagating pulse reach its minimum width after a self-focusing propagation length (see Appendix A):

$$L_C = -\text{sgn}(\beta_2)\frac{C}{1+C^2}L_D \tag{1}$$

with β_2 (with units of ps^2/km) is the GVD of the optical fiber, and $L_D = T_0^2/|\beta_2|$ is the dispersion length (expressed in km). The maximum attainable compensation length is $L_c = L_D/2$ obtained with $C = 1$.

In order to quantify the effectiveness of Graphene pre-chirping we performed a set of transmission numerical simulations. We used a pseudo-random bit sequence (PRBS) of 256 NRZ pulses at a bit rate of 10 Gb/s, with a roll-off factor of 0.2. An electrical band-pass filter was used to smooth the NRZ pulse edges and to emulate the actual optical signals attainable with the fabricated modulator. Typical values of 3-dB filter bandwidth giving optimal pre-chirping operations were found to be in the range of 0.4 to 0.8 times the bit rate of the transmission (from 4 to 8 GHz), this fit well with the fabricated modulator having 5 GHz 3-dB bandwidth. On the contrary, NRZ pulses with sharp edges (very large modulation bandwidth) are much more prone to inter-symbolic interference (ISI) giving a shorter achievable compensation distance [23]. In the simulations, we used the numerical results of Fig. 1(a) and the experimental measurements of Figs. 2(b) and 3 to define the filtered NRZ pulse amplitudes and phases.

The Beam-Propagation-Method described in [22] was used with GVD $\beta_2 = -21.6$ ps^2/km at 1550nm (typical value for standard SMF-28 step-index fibers). For comparison, the simulations were performed both in the presence and in the absence of the electrical low pass filter. Results are shown in Fig. 4.
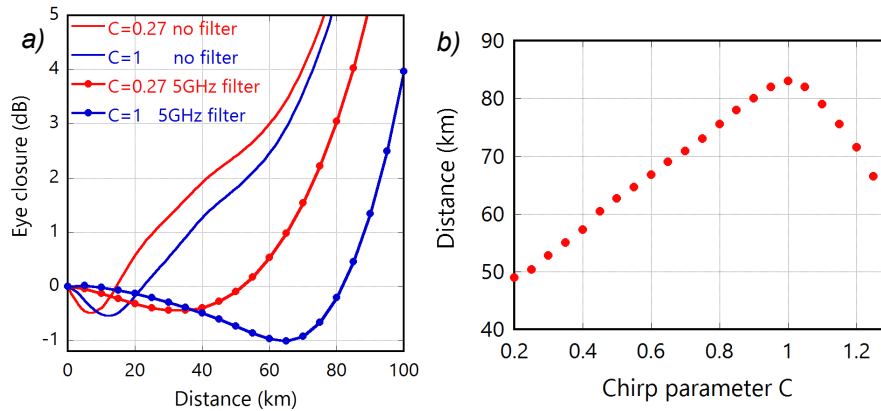

Fig. 4. (a) Eye closure penalty for NRZ transmission at 10 Gb/s over standard SMF for different values of the pre-chirp parameter C, in the absence (solid lines) and presence (dashed lines and filled circles) of a 5 GHz band-pass electrical pre-filter. Red and blue curves are for chirp parameters $C = 0.27$ and $C = 1$, respectively. (b) Zero-penalty distance versus pre-chirping parameter C.

The solid lines in Fig. 4(a) represent eye closure penalty [25, 26] for $C = 0.27$ (red lines) and $C = 1.0$ (blue lines). In the absence of electrical filtering, the pre-chirp induces a very moderate improvement to the transmission due to the steep rising and falling edges of pulses (solid lines): the interplay between high frequencies associated to these steep leading and trailing fronts and the fiber GVD cause rapid closure of the eye diagram. A dramatic improvement is observed in presence of the electrical pre-filter, which reduces the steepness of the edge fronts of the NRZ pulses, allowing for extended compensation lengths (dashed lines and filled circles). For these simulations, we used a 5 GHz low-pass electrical pre-filter to emulate the bandwidth of the fabricated EAM. In the case of $C = 0.27$, corresponding to the value used to fit the experimental instantaneous frequency of Fig. 2(b), we observe a focusing length (minimum eye closure) of 35 km. Figure 4(b) shows the 0 dB eye closure distance as a function of the pre-chirping parameter C in the presence of the electrical filter, this is about 52 km for $C = 0.27$.

We experimentally verified the compensation properties of the fabricated Si EAM thanks to a transmission experiment at 10 Gb/s over standard SMF spools of different length having dispersion $D = 17$ ps/nm/km ($\beta_2 = -21.6$ ps^2/km) (see Appendix B for details on the experimental set-up). Figure 5 summarizes the results obtained at 1550 nm: in Fig. 5(a), the back-to-back eye diagram obtained for $V_{pp} = 2.7$ V, $V_{bias} = -1$V and a 2^{31}-1-long PRBS is reported. Figure 5(b) shows the extinction ratio (ER) of the EAM as a function of the peak-to-peak driving voltage, V$_{pp}$, showing that ER = 4.5 dB can be obtained at V$_{pp}$ = 6V (all results reported in Fig. 5 are obtained at −1V bias voltage). Figure 5(b) shows that by increasing the peak-to-peak driving voltage the ER tends to saturate because the change in the transmission reaches the maximum transparency. This is in agreement with the numerical results of Fig. 1(a).

The bit error rate (BER) curves versus the optical signal to noise ratio (OSNR) for $V_{pp} = 2.7$ V in back-to-back and after different propagation distances are reported in Fig. 5(c). Despite some eye closure due to the limited bandwidth of the sample, a stable output signal with 2.5 dB ER was obtained. The back-to-back sensitivity is 34 dB OSNR, but, because of the time lens effect, the signals are compressed so to have a net eye opening (see inset eye

diagrams in Fig. 5) with a corresponding sensitivity improvement. The improvement reaches its maximum at 40 km which is very close to the simulated focusing length for $C = 0.27$. The 0 dB penalty distance is about 60 km that is also in good agreement with the simulation results. At larger propagation distances the transmission penalty increases because fiber dispersion leads to pulse broadening and inter-symbol interference. Nevertheless, 100 km transmission with a BER largely lower than the conventional Reed-Solomon forward error correction (RS-FEC) threshold of 10^{-3} is possible. The evolution of the signal eye diagram in propagation can be appreciated by the insets in Fig. 5. A longer focusing distance can be obtained using either a larger driving voltage or a longer device for having a larger chirp. In particular, we can expect a focusing (eye-closure zero penalty condition) distance of 80 km with the largest attainable chirp giving rise to a maximum deviation of the instantaneous frequency of 1.8 GHz at $V_{pp} = 6$ V at $V_{bias} = -1$ V, as predicted in Fig. 4(b). This also gives the largest attainable signal, ER = 4.6 dB.
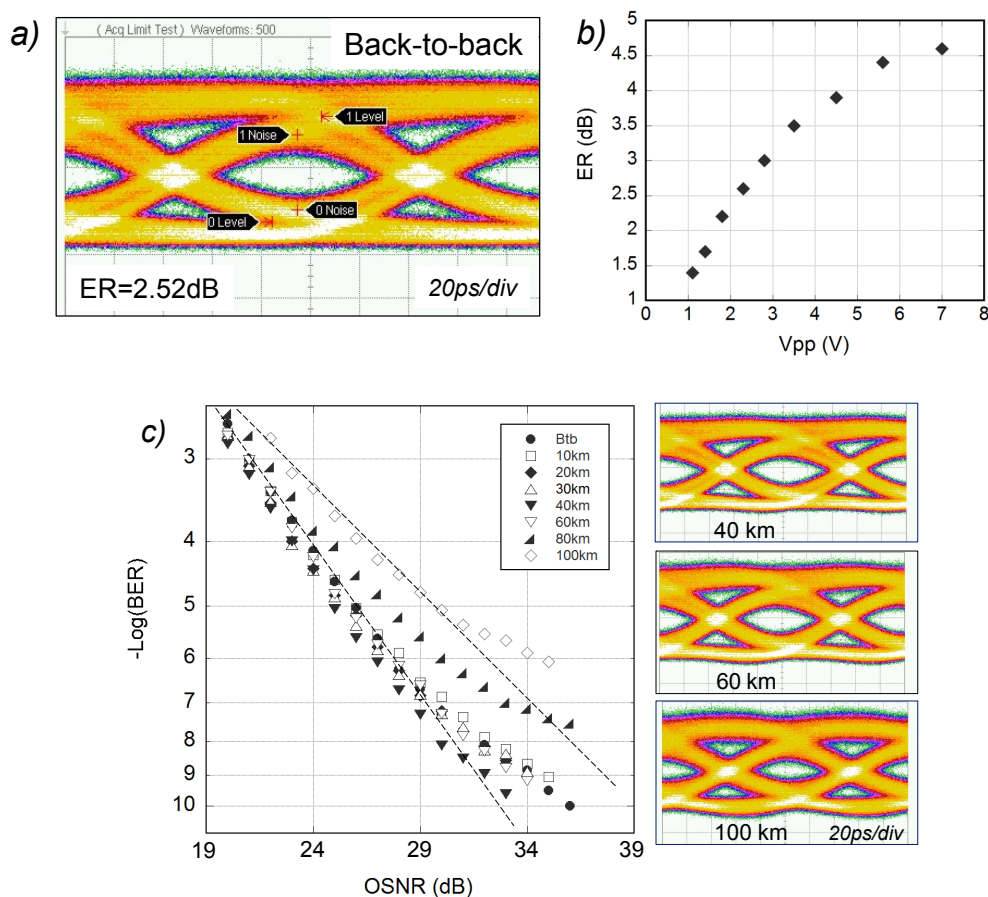

Fig. 5. (a) Back to back eye diagram for $V_{pp} = 2.7$ V. (b) ER vs. V_{pp}. (c) BER curves versus OSNR for $V_{pp} = 2.7$ V and for transmission distances up to 100 km. The insets show sample transmitted eye diagrams.

5. Conclusions

In conclusion, we studied by simulations and experiments the frequency chirp of Graphene based EAMs. We found a linear positive chirp, giving rise to a maximum deviation of the instantaneous frequency of 1.8 GHz in a 100 km-long device, and demonstrated how this linear chirp can be used to compensate for chromatic dispersion of SMFs thanks to the time-

lensing effect. With 2.7 V peak to peak driving voltage only, we showed that is possible to obtain a 60 km SMF transmission with 0-dB OSNR penalty and 100 km with a BER largely lower than the RS-FEC threshold. Together with the Graphene insensitivity to temperature and ultra-wideband operation [4], those results demonstrate an additional major benefit of introducing Graphene in Si photonics circuits and optical systems.

6. Appendix A: numerical simulation of chirp in graphene modulators

Optical chirp is the time dependence of the instantaneous frequency of an optical pulse [22]. Optical chirp accumulates on a pulse when it propagates along an optical fiber and is due to group velocity dispersion (GVD) [22]. The GVD parameter is β_2 (ps^2/km). Positive/negative values of β_2 are referred to as normal/anomalous dispersion, respectively. In the C band, standard single mode fibers (SMF) exhibit anomalous dispersion, i.e. $\beta_2 < 0$. When an optical pulse is transmitted along an SMF link, it acquires negative chirping ($C < 0$), i.e. the rising edge of the pulse travels faster than the falling one, leading to pulse broadening. In an optical communication system, this leads to bit inter-symbolic interference (ISI) [22]. Compensation of the GVD can be obtained by pre-chirping with an opposite sign the optical pulses injected into the SMF. Physically, pre-chirping behaves as a temporal lens: pulses are temporally focused at the distance where fiber chirp exactly cancels out the pre-chirp.

In order to describe the main concept, we used the simplified Gaussian amplitude modulation model. Consider a Gaussian pulse at the fiber input with the pre-chirping parameter C [22]:

$$A(t, z = 0) = A_0 \exp\left(-\frac{t^2(1 - iC)}{2T_0^2}\right). \tag{2}$$

where t and z denote time and propagation distance, respectively. A_0 and T_0 are the pulse amplitude and duration, respectively. After propagation through an arbitrary distance along the dispersive fiber, the expression for the pulse complex envelope at distance z is:

$$A(t, z > 0) \propto \exp\left(-\frac{t^2}{2T_0^2} \frac{1 - iC - iC_f(z)(1 + C^2)}{(1 + C_f(z)C)^2 + C_f^2(z)}\right). \tag{3}$$

where $C_f(z) = (\beta_2 z)/T_0^2$ is the chirp introduced by the GVD of the fiber. The pulse is chirp-free at the compensation distance L_C:

$$L_C = -\frac{T_0^2}{\beta_2} \frac{C}{1 + C^2} = -\text{sgn}(\beta_2)\frac{C}{1 + C^2} L_D. \tag{4}$$

where $L_D = T_0^2/|\beta_2|$ is referred to as the dispersion length (measured in km) [22]. At the compensation distance, the expression for the complex envelope of the propagating pulse simplifies to:

$$A(t, L_C) \propto \exp\left(-\frac{t^2}{2T_0^2}(1 + C^2)\right). \tag{5}$$

showing that the pulse compresses at the compensation distance from its initial value T_0 down to $T_0/\sqrt{1 + C^2}$.

The maximum compensation distance is obtained for a pre-chirping parameter $C = 1$, i.e. $max(L_C) = 0.5 L_D$. Observe in eq.(S3) that positive chirping $C > 0$ is needed in order to obtain temporal focusing in the presence of anomalous dispersion as in standard SMF.

Electro-absorption modulators (EAMs) based on Graphene on silicon waveguide, as the one proposed in the present work, introduce the needed positive chirp. Panel (a) of Fig. 1

shows the simulated transmission and effective index at λ = 1550nm of the optical mode travelling in the Si ridge waveguide coated by one layer of graphene, as a function of the voltage $|V\text{-}V_{DIRAC}|$ applied between the graphene layer and the waveguide. V_{DIRAC} is the flat-band voltage corresponding to the charge-neutral Dirac Point. The curves are obtained using the numerical approach discussed in [21] with a scattering parameter of 100fs. The device cross section is shown in the inset. A commercial-grade simulator eigenmode solver and propagator was used to perform the calculations [27].

When the voltage is applied to the graphene EAM, the transmission increases while the effective index of the optical mode decreases. Therefore, when a pulse is created, the phase of the optical beam at the output of the modulator is smaller on the pulse peak than on the tails. Assuming that the transit time of the pulse through the modulator is much shorter than the duration of the pulse itself, and assuming a Gaussian pulse, the phase of the pulse at the EAM output can be written as:

$$\varphi(t) = \varphi_0 + \frac{2\pi L}{\lambda_0} \Delta n_{eff}(t) \approx \varphi_0 + \frac{2\pi L}{\lambda_0} \Delta n_{max} \exp\left(-\frac{t^2}{2T_0^2}\right). \tag{6}$$

where φ_0 is an arbitrary phase, λ_0 is the free-space wavelength, and Δn_{max} is the maximum variation of the effective index obtained when driving the modulator to minimum absorption, L is the modulator length. Equation (6) is valid in the assumption of a linear dependence of the effective index change versus applied voltage. From panel a) of Fig. 1, this is a good approximation when graphene is biased above 0.4eV Fermi level corresponding to the Pauli blocking threshold at 1550nm [21].

According to Eq. (6), the instantaneous frequency deviation of the pulse at the output of the EAM is:

$$\Delta f_{inst}(t) = \frac{1}{2\pi} \frac{\partial \varphi(t)}{\partial t} = -\frac{t}{2T_0^2} \frac{L}{\lambda_0} \Delta n_{max} \exp\left(-\frac{t^2}{2T_0^2}\right). \tag{7}$$

In our experimental set-up, L = 100µm, λ_0 = 1550 nm and T_0 = 54ps. Figure 3(b) shows the experimental data, amplitude profile (left axis) and instantaneous frequency deviation (right axis), as measured with a complex spectrum analyzer (Apex AP2440), for a pulse obtained at the output of the EAM driven with a peak-to-peak voltage V_{pp} = 2.7V. We used Eq. (7) to fit the experimental instantaneous frequency deviation (red line in Fig. (5)), the fitting was obtained with $\Delta n_{max} \approx$ -0.67x10^{-3}.

The above values of maximum index change have been verified by directly measuring the instantaneous phase delay acquired by the pulse travelling through the modulator. Figure 3(a) shows the results. The blue dashed line is the instantaneous phase, showing a maximum 13.5 degrees phase displacement through the $L = 100$µm long device. This corresponds to an equivalent effective refraction index change of about -0.6x10^{-3}, very close to the fitting value.

The chirp parameter C introduced by the EAM modulator can be obtained by comparing the instantaneous frequency derived from Eq. (2):

$$\Delta f_{inst}(t) = \frac{1}{2\pi} C \frac{t}{T_0^2}. \tag{8}$$

and the instantaneous frequency derived from Eq. (6) linearized nearby the pulse peak value:

$$\Delta f_{inst}(t) = -\frac{L}{\lambda_0} \Delta n_{max} \frac{t}{T_0^2}. \tag{9}$$

The chirp parameter can be written as:

$$C = -2\pi \frac{L}{\lambda_0} \Delta n_{max} . \tag{10}$$

From the fitting of Fig. 5, we estimate a chirp parameter of 0.27 when the EAM is driven with a peak-to-peak voltage $V_{pp} = 2.7V$.

7. Appendix B: experimental setup

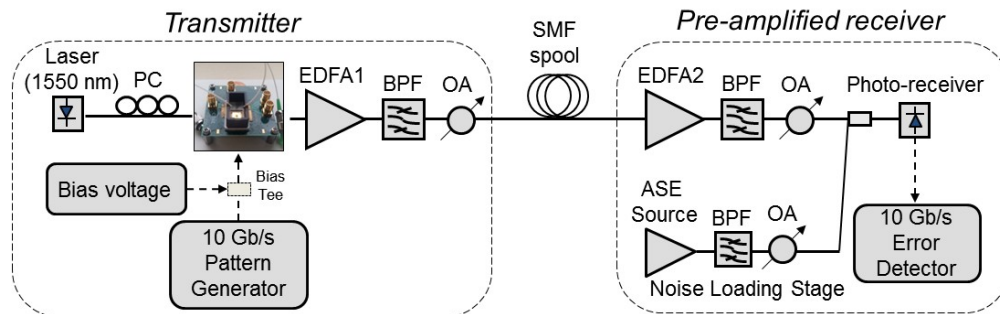The transmission was performed with the set-up of Fig. 6.

Fig. 6. Experimental setup for the transmission through SMF spools.

We used an external cavity laser (ECL) at 1550nm as the light source. The optical signal is coupled into the chip through grating couplers designed for the transverse electric (TE) fundamental mode of the Si waveguide. In order to maximize the light coupling an external polarization controller is used. The EAM is electrically driven by a 10Gb/s pattern generator through a Bias Tee used to decouple the DC bias voltage from the RF power. We used an NRZ 2^{31}-1-long PRBS with a peak-to-peak voltage of $2.7V_{pp}$. The EAM is biased at $-1V$. The modulated optical signal at the output of the chip was amplified by an erbium doped fiber amplifier (EDFA), to compensate for the chip insertion loss (about $-19dB$ mainly due to the grating couplers efficiency and propagation loss of the air cladded Si waveguides).

The amplified optical signal is then filtered by an optical band pass filter (BPF) with a bandwidth of 1nm to reduce the optical noise introduce by the amplifier. A variable optical attenuator (OA) was also used to control the optical power at the input of the fiber spool. We used SMF spools of different length, from 10 up to 100km, having dispersion D=17 ps/nm/km (β_2=-21.6 ps^2/km). At the output of the SMF spool, in particular for the longer distances, we put another set of EDFA, BPF and OA to compensate the fiber propagation loss. A noise loading stage based on amplified spontaneous emission (ASE) source, a BPF and OA, was used to perform the bit error rate (BER) measurement versus optical signal to noise ratio (OSNR). The noise loaded optical signal was collected with a photo-receiver and analyzed with an error detector.